JACS
JOURNAL OF THE AMERICAN CHEMICAL SOCIETY
Article
Cite This: J. Am. Chem. Soc. 2019, 141, 6292−6301
pubs.acs.org/JACS

Dual Photocatalytic Roles of Light: Charge Separation at the Band Gap and Heat via Localized Surface Plasmon Resonance To Convert CO_2 into CO over Silver−Zirconium Oxide

Hongwei Zhang,[†] Takaomi Itoi,[‡] Takehisa Konishi,[†] and Yasuo Izumi*[,†]

[†]Department of Chemistry, Graduate School of Science, Chiba University, Yayoi 1-33, Inage-ku, Chiba 263-8522, Japan
[‡]Department of Mechanical Engineering, Graduate School of Engineering, Chiba University, Yayoi 1-33, Inage-ku, Chiba 263-8522, Japan

Supporting Information

ABSTRACT: Confirmation of $^{13}CO_2$ photoconversion into a ^{13}C-product is crucial to produce solar fuel. However, the total reactant and charge flow during the reaction is complex; therefore, the role of light during this reaction needs clarification. Here, we chose Ag−ZrO_2 photocatalysts because beginning from adventitious C, negligible products are formed using them. The reactants, products, and intermediates at the surface were monitored via gas chromatography−mass spectrometry and FTIR, whereas the temperature of Ag was monitored via Debye−Waller factor obtained by in situ extended X-ray absorption fine structure. With exposure to $^{13}CO_2$, H_2, and UV−visible light, ^{13}CO selectively formed, while 8.6% of the ^{12}CO mixed in the product due to the formation of ^{12}C-bicarbonate species from air that exchanged with the $^{13}CO_2$ gas-phase during a 2 h reaction. By choosing the light activation wavelength, the CO_2 photoconversion contribution ratio was charge separated at the ZrO_2 band gap (λ < 248 nm): 70%, localized at the Ag surface plasmon resonance (LSPR) (330 < λ < 580 nm): 28%, and characterized by a thermal energy of 295 K: 2%. LSPR at the Ag surface was converted to heat at temperatures of up to 392 K, which provided an efficient supply of activated H species to the bicarbonate species, combined with separated electrons and holes above the ZrO_2, which generated CO at a rate of 0.66 μmol h^{-1} g_{cat}^{-1} with approximately zero order kinetics. Photoconversion of $^{13}CO_2$ using moisture was also possible. Water photo-oxidation step above ZrO_2 was rate-limited, and the side reactions that formed H_2 above the Ag were successfully suppressed instead to produce CO via the Mg^{2+} addition to trap CO_2 at the surface.

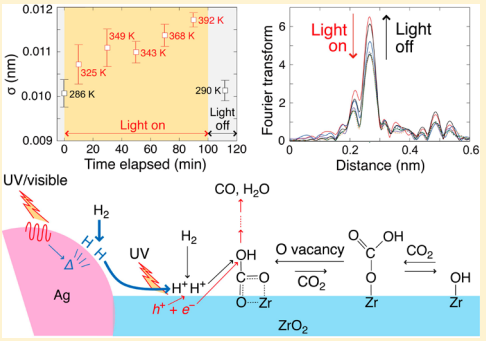

1. INTRODUCTION

Numerous studies have investigated photocatalytic CO_2 fuel conversion to initiate a carbon-neutral cycle, which includes the use of solar fuel in contrast to the irreversible consumption of fossil fuels.[1,2] However, pitfalls exist in these previous investigations that mistake methane and/or C-containing products converted from catalyst impurities as products converted from CO_2.[1,3−6] Therefore, finding an effective photocatalyst to convert CO_2 (standard formation enthalpy = −393.5 kJ mol^{-1}) using only sustainable energy while confirming labeled $^{13}CO_2$ conversion, not adventitious C, is essential.[1,3,6−12]

Previous studies have rarely used time course monitoring for isotope labeled-$^{13}CO_2$ to confirm CO_2 conversion. This study monitors the $^{13}CO_2$ photoreduction time course and investigates the ^{13}C and ^{12}C product origins. On the basis of this mechanistic investigation, we observe and clarify the dual roles that UV−visible light has for the first time using ZrO_2-based photocatalysts:[13−15] (i) charge separation at the band gap (BG) and (ii) heat transformed via localized surface plasmon resonance (LSPR) via extended X-ray absorption fine structure (EXAFS). Temperature monitoring of the Ag via Debye−Waller factor, which was obtained with in situ EXAFS, was direct in comparison with surface-enhanced Raman techniques that use adsorbed probe molecules.

First, this study evaluates the rates of step 2 that follows water photo-oxidation in step 1 below.[16−18]

$$2H_2O \rightarrow O_2 + 2H_2 \text{ (or } 4H^+ + 4e^-), \quad \Delta_r H^\circ = 483.64 \text{ kJ mol}^{-1} \tag{1}$$

$$CO_2 + H_2 \text{ (or } 2H^+ + 2e^-) \rightarrow CO + H_2O, \quad \Delta_r H^\circ = 41.16 \text{ kJ mol}^{-1} \tag{2}$$

$$CO_2 + H_2O \rightarrow CO + O_2 + H_2, \quad \Delta_r H^\circ = 524.80 \text{ kJ mol}^{-1} \tag{3}$$

Received: January 4, 2019
Published: March 27, 2019

DOI: 10.1021/jacs.8b13894
J. Am. Chem. Soc. 2019, 141, 6292−6301

We analyzed the photocatalytic mechanism in step 2, and we also attempted the photoconversion of $^{13}CO_2$ using moisture (step 3).

2. EXPERIMENTAL METHODS

An aqueous Ag nitrate (>99.8%, Wako Pure Chemical, Japan) solution was reduced in a liquid phase using $NaBH_4$ (>95%, Wako Pure Chemical) in the presence of ZrO_2 (JRC-ZRO-3, Catalysis Society of Japan; tetragonal phase, specific surface area = 94.4 $m^2 g^{-1}$).[17] We varied the sample Ag content between 0.50 and 10 weights (wt) %. The sample is denoted as Ag−ZrO_2. Mg nitrate (>99.5%, Wako Pure Chemical) was impregnated into the Ag−ZrO_2 aqueous suspension. The molar ratio of Mg:Ag was 1:1. The water was distilled at 358 K, and the powder product was dried at 373 K for 40 h.

The photocatalyst (0.100 g) was placed in a quartz photoreactor and evacuated at 295 K for 2 h while connected to a Pyrex glass circulation system (206.1 mL) and both rotary and diffusion pumps (10^{-6} Pa).[16] We then introduced 2.3 kPa of $^{13}CO_2$ (^{13}C 99.0%, ^{17}O 0.1%, ^{18}O 0.7%, chemical purity >99.9%, Cambridge Isotope Laboratories, Inc., Tewksbury, MA, USA) and 21.7 kPa of H_2 (>99.99%). For comparisons, the pressure of $^{13}CO_2$ and H_2 was varied in the ranges 1.1−6.7 kPa and 21.7−66.7 kPa, respectively. The reactor catalyst was irradiated with UV−visible light from a 500 W xenon arc lamp (Model OPM2−502, Ushio, Japan). The distance between the UV−visible light exit and the photocatalyst was 20 mm. The light intensity was 90.2 mW cm^{-2} at the center of the photocatalyst. The intensity distribution of the Xe arc lamp was measured using a spectroradiometer (Model USR45DA, Ushio, Japan) at a position 20 mm apart from the UV−visible light exit (Figure S1, Supporting Information). A small portion of distribution lower than λ = 248 nm exists enabling the BG excitation of ZrO_2. In-profile kinetic data were collected as a function of the light's excitation wavelength by inserting a sharp-cut filter (2.5 mm thick) at the lighthouse exit. We used the UV32 and O58 (Hoya, Japan) types to pass light with λ > 320 nm and λ > 580 nm, respectively.[19,20] Control tests with exposure to $^{13}CO_2$, H_2, and no light were performed by completely wrapping the reactor with Al foil. We also performed control tests with exposure $^{13}CO_2$ gas only and UV−visible light. The exchange reaction with 0.67 kPa of $^{13}CO_2$ was also performed using a similar procedure.

A packed column of 13X-S molecular sieves (3 m length, 3 mm internal diameter; GL Sciences, Inc., Japan) was employed for online gas chromatography−mass spectrometry analyses (GC−MS; Model JMS-Q1050GC, JEOL, Japan).[21−23] Helium (purity >99.9999%) was used as the carrier gas at 0.40 MPa. The sampling loop comprised a Pyrex glass system kept under vacuum using rotary and diffusion pumps (10^{-6} Pa) connected to the GC−MS via 1.5 m deactivated fused silica tubes (No. 160-2845-10, Agilent, Santa Clara, CA, USA; internal diameter 250 μm), which were maintained at 393 K during analysis to avoid gas adsorption.

The surface species were monitored with a single-beam Fourier transform infrared (FTIR) instrument (JASCO, Japan; Model FT/IR-4200) equipped with a mercury−cadmium−tellurium-M detector at a constant temperature of 77.4 K.[24] A 20 mm-Φ self-supporting disk of ZrO_2 or Ag (5.0 wt %)−ZrO_2 disk (50 mg) was placed in a quartz photoreaction cell equipped with NaCl windows on both sides. The photoreaction cell was connected to the Pyrex glass circulation system as well as the GC−MS to enable simultaneous surface species monitoring via FTIR and isotope distribution in the gas with the GC−MS. The photocatalyst disk was evacuated (10^{-6} Pa) at 295 K for 2 h prior to FTIR and GC−MS measurements.[16]

In situ FTIR measurements were performed at 295 K in a range from 4000 to 650 cm^{-1}. The sample disk was irradiated with UV−visible light from a 500 W Xe arc lamp using quartz fiber light guide (San-ei Electric Co., Japan; Model 5Φ-2B-1000L). The distance between the fiber light exit and sample disk was 50 mm. The light intensity at the center of sample was 88 mW cm^{-2}. The spectrometer's energy resolution was 1 cm^{-1}. A 10%-cut filter was inserted in front of the photoreaction cell. Data accumulation was between 128 and 256 scans (approximately 2 s per scan).

UV−visible spectra were recorded on a double-beam model V-650 spectrophotometer using D_2 and halogen lamps below and above 340 nm equipped with a photomultiplier tube and an integrated ISV-469 sphere (JASCO) to diffuse reflectance detection within the range from 200 to 800 nm.[16,23] Data was transformed using the Kubelka−Munk function. A formed polytetrafluoroethylene plate was used as a reference. Absorption−fluorescence spectra were recorded on model FP-8600 (JASCO; Chiba Iodine Resource Innovation Center, Chiba University) using 150-W Xe arc lamp equipped with a photomultiplier tube within the excitation range from 200 and 300 nm and fluorescence range from 300 to 800 nm.

Silver K-edge EXAFS spectra were measured at 290 K in transmission mode at the Photon Factory Advanced Ring, High Energy Accelerator Research Organization (KEK, Tsukuba, Japan) on the NW10A beamline.[25] A Si(3 1 1) double-crystal monochromator and a Pt-coated focusing cylindrical mirror were inserted into the path of the X-ray beam. A Piezo transducer was used to detune the X-ray to two-thirds of the maximum intensity to suppress higher harmonics. The Ag K-edge absorption energy was calibrated at 25516.5 eV using the X-ray spectrum of a Ag metal foil (40 μm thick).[26] A disk (Φ = 10 mm) of a Ag (3.0−5.0 wt %)−ZrO_2 photocatalyst (125 mg) was set in a Pyrex glass reactor equipped with a Kapton film (Dupont, Wilmington, DE, USA; 50 μm thick) for X-ray transmission and a polyethylene terephthalate (PET) film (Teijin, Japan, G2; 50 μm thick) for both UV−visible light and X-ray transmission filled with 2.3 kPa of CO_2 and 21.7 kPa of H_2. The sample was irradiated with UV−visible light from a Xe arc lamp through the PET film at the beamline.[18,24,27,28]

The obtained Ag K-edge EXAFS data were analyzed using the XDAP software package.[29] The pre-edge background was approximated with a modified Victoreen function, i.e., $C_2/E^2 + C_1/E + C_0$, where E is the photon energy. The background for postedge oscillation, μx, was approximated with a smoothing spline function and was calculated for a particular number of data points:

$$\sum_{i=1}^{\text{Data Points}} \frac{(\mu x_i - \text{background}_i)^2}{\exp(-0.075k_i^2)} \leq \text{smoothing factor} \quad (4)$$

where k is the angular photoelectron wavenumber.

Multiple-shell curve fit analyses were performed on the Fourier-filtered k^3-weighted EXAFS data in k- and R-space (R: interatomic distance) using the empirical amplitude extracted from the EXAFS data for the Ag metal foil (40 μm thick). The R and coordination number (N) values for the Ag−Ag interatomic pair were set to 0.288 9 nm and 12.[30] We assumed that the many-body reduction factor, S_0^2, is identical for both the sample and reference.

The high-resolution transmission electron microscopy (HR-TEM) investigations were performed using a JEM-2100F (JEOL) equipped with a field emission gun at an acceleration voltage of 200 kV.[27] The samples were mounted on a Cu mesh (250 mesh per inch) coated with a copolymer film of poly(vinyl alcohol) and formaldehyde (Formvar, Monsanto, St. Louis, MO, USA) and coated with carbon. Chemical compositions and elemental distributions were analyzed using energy dispersive spectra equipped with a Si(Li) detector in the TEM.

3. RESULTS AND DISCUSSION

We first compared the reactions exposed to CO_2 and H_2 using several ZrO_2-based photocatalysts doped with varying amounts of Ag under UV−visible light irradiation (Table 1A-a−e and Figure S2). The major product using these catalysts was always CO. The formation rate using 5.0 wt % Ag−ZrO_2 (0.57 μmol h^{-1} g_{cat}^{-1}) was higher by a factor of 3.9 than when using ZrO_2 (0.15 μmol h^{-1} g_{cat}^{-1}; Table 1A-a, d). When the photocatalyst Ag content varied between 0.50 and 10 wt %, we were able to maximize the total CO formation rate by using Ag (5.0 wt %)−

DOI: 10.1021/jacs.8b13894
J. Am. Chem. Soc. 2019, 141, 6292−6301

Table 1. Kinetic Data on Photoconversion of CO_2 Using the ZrO_2-Based Photocatalyst under UV−Visible Light

(A) $^{13}CO_2$ (2.3 kPa) and H_2 (21.7 kPa)

entry	catalyst	light irradiated	formation rate (μmol h^{-1} g_{cat}^{-1}) ^{13}CO	^{12}CO
a	ZrO_2	Full light	0.10	0.045
a′		λ > 320 nm	0.018	0.0084
b	Ag (0.50 wt %)−ZrO_2	Full light	0.20	0.11
c	Ag (3.0 wt %)−ZrO_2	Full light	0.38	0.079
d	Ag (5.0 wt %)−ZrO_2	Full light	0.52	0.049
d′		λ > 320 nm	0.15	0.017
d′′		λ > 580 nm	0.0093	0.0034
e	Ag (10 wt %)−ZrO_2	Full light	0.46	0.065

(B) $^{13}CO_2$ (2.3 kPa) and H_2O (2.7 kPa)

entry	catalyst	formation rate (μmol h^{-1} g_{cat}^{-1}) ^{13}CO	^{12}CO	H_2
a	ZrO_2	0.018	0.16	0.074
b	Ag (5.0 wt %)−ZrO_2	0.0031	0.0049	0.15
c	Mg^{2+}−Ag (5.0 wt %)−ZrO_2	0.0010	0.092	<0.002

(C) Pressure Dependence of CO Formation Rate Using $^{13}CO_2$, H_2, and Ag (5.0 wt %)−ZrO_2

formation rate of ^{13}CO (μmol h^{-1} g_{cat}^{-1}) / formation rate of ^{12}CO (μmol h^{-1} g_{cat}^{-1})	H_2 pressure (kPa) 0	21.7	43.8	66.7
$^{13}CO_2$ pressure (kPa)				
1.1		0.39		
		0.045		
2.3	<0.0009	0.52	0.59	0.52
	<0.001	0.049	0.049	0.033
4.8			0.61	
			0.034	
6.7		0.50		0.62
		0.035		0.036

ZrO_2 (Table 1A-a−e and Figure S3). We confirmed the predominant photocatalytic formation of ^{13}CO, which was derived from $^{13}CO_2$. However, minor ^{12}CO also formed continuously (Figures 1A and S2). Caution should be exercised for formation rates of CO that are of the order of μmol h^{-1} g_{cat}^{-1}; the rates of tens of mmol h^{-1} g_{cat}^{-1} have been reported for methane formation.[2,31] The differences of reaction conditions, products, and their associated free energy change must be carefully considered; however, this study isotopically clarifies the mechanism from CO_2 to CO activated by light in the course of time.

The ^{13}CO and ^{12}CO formation rates using Ag (5.0 wt %)−ZrO_2 were 0.52 μmol h^{-1} g_{cat}^{-1} and 0.049 μmol h^{-1} g_{cat}^{-1}, respectively (Figure 1A). The ^{12}C ratio in reactant CO_2 was 1.0%, whereas the ^{12}C ratio in formed CO was 8.6% (Table 1A-d). To understand this inconsistency, we performed a $^{13}CO_2$ (0.67 kPa) exchange reaction with Ag (5.0 wt %)−ZrO_2 under UV−visible light irradiation (Figure 2B). The exchange reaction proceeded with $^{12}CO_2$, which was adsorbed from air and remained after pretreatment under vacuum. The exchange reaction reached equilibrium after 2 h. We assumed that this reaction followed the first-order kinetics and that the rate constants, k_r and k_r', are the exchange between gas-phase $^{13}CO_2$ with adsorbed $^{12}CO_2$ and gas-phase $^{12}CO_2$ with adsorbed $^{13}CO_2$, respectively.

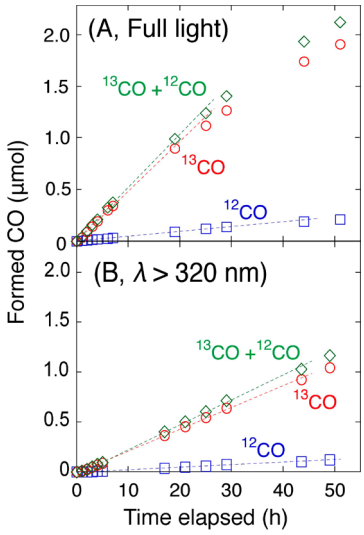

Figure 1. Time course formation of photocatalytic ^{13}CO and ^{12}CO during exposure to $^{12}CO_2$ (2.3 kPa) and H_2 (21.7 kPa) using Ag (5.0 wt %)−ZrO_2(0.100 g) irradiated by (A) full UV−visible light and (B) filtered light at λ > 320 nm.

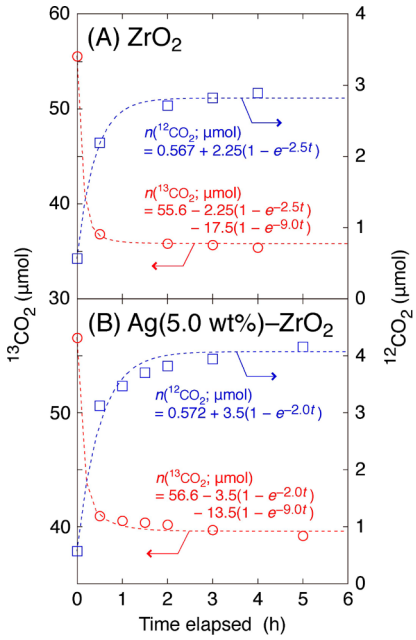

Figure 2. Time course exchange reaction of $^{13}CO_2$ (0.67 kPa) irradiated by UV−visible light using (A) ZrO_2 and (B) Ag (5.0 wt %)−ZrO_2. Photocatalyst used was 0.100 g.

$$\frac{dP_{^{13}CO_2}}{dt} = -k_r P_{^{13}CO_2} + k_r' P_{^{12}CO_2} \quad (5)$$

$$P_{^{13}CO_2} + P_{^{12}CO_2} = P_{^{13}CO_2(initial)} \quad (6)$$

$$\therefore P_{^{12}CO_2} = P_{^{12}CO_2(equilibrium)}\{1 - e^{-(k_r + k_r')t}\} \quad (7)$$

On the basis of the fit (Figure 2B), the sum of the rate constants (k_r + k_r') required to attain an exchange equilibrium was 2.0 h^{-1}. A quicker reaction of 13.5 μmol $^{13}CO_2$ along the free sites of the Ag (5.0 wt %)−ZrO_2 surface had a rate constant of 9.0 h^{-1} in comparison to the $^{13}CO_2/^{12}CO_2$ exchange (3.5 μmol). The converged $^{12}CO_2$ partial pressure

DOI: 10.1021/jacs.8b13894
J. Am. Chem. Soc. 2019, 141, 6292−6301

in total CO_2 was 9.3%, which is in good agreement with the ^{12}C ratio that formed in the CO (8.6%). We also performed the exchange test when exposed to dark conditions (Figure S4B). The total $^{13}CO_2$ uptake changed negligibly. However, the amount of exchangeable $^{13}CO_2/^{12}CO_2$ was greater by a factor of 1.46 when exposed to light (Figures S4B and 2B), which suggests that the CO_2-derived species is light activated. ^{13}CO began to form after an induction period of 0.5 h due to an exchange delay with the ^{12}C surface species (Figure S2, Left), as well as the Ag activation via heating by light (see below).

Using ZrO_2 (Figure 2A), the converged partial pressure of $^{12}CO_2$ in the total CO_2 was 7.3%, whereas the ^{12}C ratio in the total CO was as high as 27% (Table 1A-a and Figure S2A), which suggests the existence of an irreversible CO_2-derived species leading to CO formation associated with O vacancy in ZrO_2 (2.3 μmol, Figure 2A and Scheme 1c).[32,33] The uptake of

Scheme 1. Proposed Intermediate Species Starting from CO_2 and H_2 to CO during CO_2 Exchange and Photocatalytic CO_2 Reduction

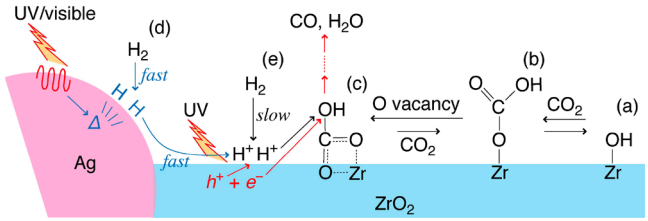

O atoms at the O vacancy site in ZrO_2 correlated well with the intensity ratio between the Zr 3d and O 1s peaks in the X-ray photoelectron spectra.[34,35] The O vacancy was more reactive in Ag–ZrO_2 when exposed to UV–visible light due to H activation by Ag (3.5 μmol, Figure 2B), whereas we observed no Ag effects when exposed to dark conditions (Figure S4A,B). The number of total CO_2-derived sites on the ZrO_2 (0.100 g) surface was 1.3 CO_2 molecules per nm^2, which decreased to 1.1 CO_2 molecules per nm^2 of Ag–ZrO_2 (Figure 2). This demonstrates that CO_2-derived species were above the ZrO_2 surface and not above Ag.

The rate dependence on reactant pressure approaching atmospheric pressure was also studied using Ag (5.0 wt %)–ZrO_2 catalysts (Table 1C). Extremely weak dependence on both the pressure of CO_2 and H_2 was found with a maximum CO formation rate of 0.66 μmol h^{-1} g_{cat}^{-1} at 6.7 kPa CO_2 and 66.7 kPa H_2, demonstrating approximately zero order kinetics due to the strong adsorption of CO_2 and H.

FTIR spectra were measured for the ZrO_2 pretreated under vacuum at 295 K for 2 h. With the adsorption of CO_2 at 295 K for 2 h, peaks appeared at 1624, 1421, and 1220 cm^{-1}, which were assigned to bicarbonate species (monodentate or bridging; Figure 3A1, Left).[36] Simultaneously, the ZrO_2 hydroxy peak at 3700 cm^{-1} decreased due to a reaction with CO_2 while the bicarbonate hydroxy peak increased at 3615 cm^{-1} (Figure 3A1, Right). Much weaker shoulder peaks, due to carbonate species, also appeared at 1553 and 1334 cm^{-1}.[37] When exposed to vacuum for 30 s and 7 min, the peaks, due to the bicarbonate species, decrease by 1/2–2/3 (Figure 3A2, 3, Left). Since carbonate species were present in the pretreated sample under vacuum (data not shown), the changes under

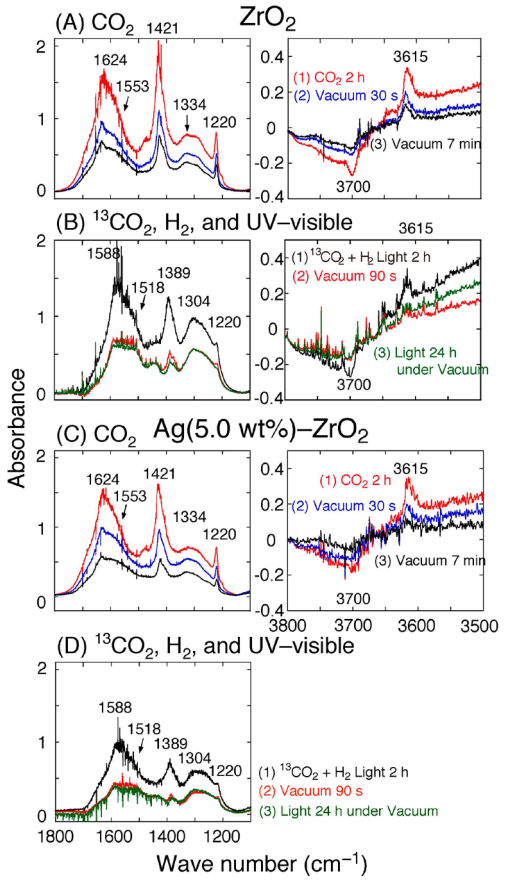

Figure 3. FTIR spectra of ZrO_2 (50 mg; A, B) and Ag (5.0 wt %)–ZrO_2 (50 mg; C, D). (A, C) Under CO_2 for 2 h (1) and under vacuum for 30 s (2) and 7 min (3). (B, D) Under UV–visible light, $^{13}CO_2$ (2.3 kPa), and H_2 (21.7 kPa) for 2 h (1) and under vacuum for 90 s (2) and 24 h (3).

both CO_2 and vacuum were minimal and we, therefore, regard carbonate as inert.

We then monitored FTIR changes associated with UV–visible light irradiation (Figure 3B). At 2.3 kPa of $^{13}CO_2$ and 21.7 kPa of H_2 irradiated by UV–visible light for 2 h, the background level, e.g., the level in the wavenumber region of 3650–3500 cm^{-1}, increased as a result of the IR excitation of UV–visible-excited electrons trapped beneath the conduction band of ZrO_2 (Figure 3B2,3),[27,38] while the vibrational peaks of surface species showed negligible change before and after irradiation by UV–visible light. A similar trapping state in CdSe during IR excitation and further hot electron injections from LSPR Au nanoparticles were reported.[39] The antisymmetric and symmetric stretching vibration peaks at 1624 and 1421 cm^{-1} for bicarbonate and at 1553 and 1334 cm^{-1} for carbonate in natural CO_2 (Figure 3A, Left) shifted to 1588 and 1389 cm^{-1} and 1518 and 1304 cm^{-1} in $^{13}CO_2$ and H_2 (Figure 3B, Left), respectively, based on the following equation for harmonic oscillation:[24]

$$\tilde{\nu} = \frac{1}{2\pi c}\sqrt{\frac{k}{\mu}} \tag{8}$$

$$\frac{\tilde{\nu}_{^{13}CO}}{\tilde{\nu}_{^{12}CO}} = \frac{\sqrt{\frac{1}{13}+\frac{1}{16}}}{\sqrt{\frac{1}{12}+\frac{1}{16}}} = 0.97778 \tag{9}$$

DOI: 10.1021/jacs.8b13894
J. Am. Chem. Soc. 2019, 141, 6292–6301

where $\tilde{\nu}$ is the wavenumber, c is the speed of light, k is the force constant, and μ is the reduced mass. We chose a peak at 1389 cm^{-1} to evaluate the amount of change in the bicarbonate species. Under vacuum for 90 s, the bicarbonate peaks decreased to one-third of their intensity under $^{13}CO_2$ and H_2 (Figure 3B1,2), which corresponds to the amount of exchange between $^{13}CO_2$ and $^{12}CO_2$ (2.3 μmol per 0.100 g_{cat}; Figure 2A). The chemisorbed bicarbonate species, which were exchangeable in gaseous CO_2, became bridged while the bicarbonate species desorbed under vacuum since CO_2 monodentately coordinates to the Zr site (Scheme 1b,c).[36] Similarly, isotope labeled bicarbonate exchanged with CO_2, which was monitored using attenuated total reflectance IR. Previous studies have suggested these as an intermediate to CO formation above Au.[40]

We also confirmed that the amount of exchange of CO_2 and rate constants (simple adsorption, exchange) negligibly varied between the powder (Figure 2) and disk samples (Figure 3). When exposed to vacuum and UV−visible light for 24 h, the bicarbonate peaks further decreased to 85% of their intensity under vacuum for 90 s (Figure 3B2,3). The decreased amount was

$$2.3\ \mu\text{mol} \times \frac{0.050}{0.100} \times 0.15 = 0.17\ \mu\text{mol-}^{13}CO_3H \quad (10)$$

versus ^{13}CO detected by GC−MS (0.001 9 μmol). Only 1.1% of the ^{13}C-bicarbonate species along the ZrO_2 surface photoconverted to ^{13}CO because of the simultaneous occurrence of a reverse reaction to $^{13}CO_2$. Due to the limitations of the 13X-S molecular sieve column, desorbed $^{13}CO_2$ could not be quantitatively evaluated using GC−MS and the total mass balance starting from bicarbonate was not confirmed. The amount of reduction of $^{13}CO_2$ to ^{13}CO should be related to that of surface O vacancies in ZrO_2. The effects of apparatus-based IR light on photocatalysis should be negligible because no reduction in CO_2 was observed, even in the presence of H_2 (see the following wavelength dependence section, Table 1A-d″ nor was significant amount of heat induced in comparison to LSPR-induced heat as a result of UV−visible irradiation (see the following EXAFS section, Table S2-e).

We also monitored the behavior between CO_2 and the Ag (5.0 wt %)−ZrO_2 photocatalyst using FTIR. The peak position and change in intensity during CO_2 adsorption at 295 K and subsequent evacuation (Figure 3C) were similar to the changes observed when using ZrO_2 (Figure 3A), which demonstrates that both the bicarbonate and carbonate species were above the ZrO_2 surface, not the Ag surface. A relatively greater portion of bicarbonate species remained (3/5−1/3) under vacuum for 30 s and 7 min (Figure 3C) in comparison with the ratio using the ZrO_2 (Figure 3A) in consistent with the amounts of exchanged (chemisorbed) CO_2, i.e., 2.3 and 3.5 μmol using ZrO_2 and Ag (5.0 wt %)−ZrO_2, respectively (Figure 2).

At 2.3 kPa of $^{13}CO_2$ and 21.7 kPa of H_2 with irradiation using UV−visible light for 2 h (Figure 3D), we observed a perfect isotope shift similar to the shift observed using ZrO_2 (Figure 3B and eq 9). However, the intensity of the bicarbonate peak decreased by approximately 50% when exposed to $^{13}CO_2$ and H_2 in comparison with CO_2, which suggests the presence of H_2 activation on Ag and spillover onto the ZrO_2 surface (Scheme 1d). When exposed to vacuum and UV−visible light for 24 h, the bicarbonate peaks further decreased to 89% of their intensity observed under vacuum for 90 s (Figure 3D2,3). The decreased amount was

$$3.5\ \mu\text{mol} \times \frac{0.050}{0.100} \times 0.11 = 0.19\ \mu\text{mol-}^{13}CO_3H \quad (11)$$

versus ^{13}CO detected by GC−MS (0.029 μmol). Fifteen percent of the $^{13}CO_2$ at the Ag−ZrO_2 surface photoconverted to ^{13}CO. Clearly, Ag promoted intermediate species reduction to CO associated with H supplied from Ag and O vacancy sites in comparison with the ratio (1.1%) using ZrO_2 associated with only O vacancy sites.

In the UV−visible spectra for the Ag−ZrO_2 samples, a peak centered at 428 nm was dominant between an Ag composition of 0.5 and 3.0 wt %, whereas shoulder features centered at 368 and/or 470 nm increased at elevated Ag contents, i.e., 5.0−10 wt % (Figure 4). These peaks are due to LSPR induced by

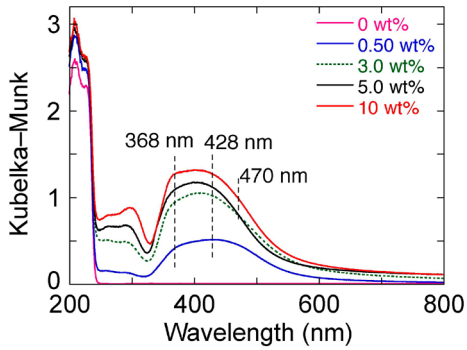

Figure 4. Diffuse reflectance UV−visible spectra for the Ag−ZrO_2 samples. The Ag contents were 0, 0.50, 3.0, 5.0, and 10 wt %.

UV−visible light where the Ag particle size distribution became wider with increased Ag content. The absorption edge was always at 248 nm (Figures 4 and S1), which indicates that the ZrO_2 BG is 5.0 eV.

As the response to UV light absorption, ZrO_2 samples showed broad and sharp fluorescence peaks at 370 and 396 nm, respectively, with excitation at 200 nm (Figure S5A-a), whereas the peaks were almost extinguished with excitation at 240 nm (Figure S5A-b). The excitation spectra for the two peaks (Figure S5B) and the wavelength dependence of the Xe arc lamp (Figure S1) suggested contribution of light at $200 < \lambda < 248$ nm to charge separation in ZrO_2 (Scheme 1). A fluorescence peak was reported for mean 4 nm-ZrO_2 with excitation at 300 nm and an extension of the excitation wavelength was ascribed to the transition involving extrinsic states.[41] Such an effect involving O vacancy states is also plausible under the conditions using H_2 and UV−visible light shown in this study (Scheme 1c).

Formation rates of CO using ZrO_2 and Ag (5.0 wt %)−ZrO_2 irradiated under full light (0.15 and 0.57 μmol h^{-1} g_{cat}^{-1}; Table 1A-a,d) decreased to 0.027 and 0.17 μmol h^{-1} g_{cat}^{-1}, respectively, under light at $\lambda > 320$ nm (Table 1A-a′,d′ and Figure 1B). The rate using Ag (5.0 wt %)−ZrO_2 irradiated by light at $\lambda > 580$ nm further decreased to 0.013 μmol h^{-1} g_{cat}^{-1} (Table 1A-d″). Therefore, for ZrO_2, the CO formation rate decreased by 82% with the filtration of the excitation light at $\lambda > 320$ nm in comparison to a photocatalytic test irradiated under full UV−visible light (Table 1A-a,a′), i.e., UV light at $\lambda < 248$ nm to separate the charges at the ZrO_2 BG (Figure 4) played a significant photocatalytic role in the reduction of CO_2

DOI: 10.1021/jacs.8b13894
J. Am. Chem. Soc. 2019, 141, 6292−6301

(82%). For the Ag (5.0 wt %)−ZrO_2, the CO formation rate decreased by 70% and 98% with the filtration of the excitation light at a $\lambda > 320$ nm and $\lambda > 580$ nm, respectively, in comparison with tests under full UV−visible light (Table 1A-d,d′,d′′). UV light at $\lambda < 248$ nm separated the charges at the ZrO_2 BG and UV−visible light at $330 < \lambda < 580$ nm induced Ag LSPR (Figures 4 and S1), which also played a significant role in the photocatalytic reduction of CO_2 (i.e., 70% and 28%, respectively).

Total CO formation rates in the blank tests when exposed to $^{13}CO_2$, H_2, and no light were 0.0062 and 0.013 μmol h^{-1} g_{cat}^{-1} using ZrO_2 and Ag (5.0 wt %)−ZrO_2, respectively (Table S1A-a,b). These rates proceeded thermally (295 K, $\frac{1}{2}RT = 1.2$ kJ mol^{-1}) but were only 4.2% and 2.2%, respectively, of the corresponding rates under UV−visible light (Table 1A-a,d). The other blank test under $^{13}CO_2$ and UV−visible light using Ag (5.0 wt %)−ZrO_2 formed no products above GC−MS detection limits (Table S1B-a).

Ag K-edge EXAFS spectra were monitored for Ag (3.0 or 5.0 wt %)−ZrO_2 under CO_2 (2.3 kPa) and H_2 (21.7 kPa) irradiated using UV−visible light at beamline. In the Fourier transform (FT; Figure 5C), a peak due to a Ag−Ag interatomic scattering of photoelectrons dominated at 0.28 nm (phase shift uncorrected), which demonstrates that the Ag nanoparticles were exclusively metallic.[25] In fact, in the HR-TEM images, we observed the metallic Ag(1 1 0) lattice fringes (i.e., the interval 0.287 nm versus the theoretical 0.289 nm[30]) to be in contact with the tetragonal ZrO_2(1 0 0) lattice fringe (i.e., the interval 0.364 nm versus the theoretical 0.364 nm; Figure 6).[42] The EXAFS FT peak intensity was significantly suppressed, i.e., by as much as 31%, during a 100 min period of light irradiation (Figure 5C). On the contrary, peak intensity quickly recovered when the light was turned off.

Such light-induced changes in the FT were quantitatively evaluated using a curve fit analysis based on the plane-wave approximation for amplitude $A_i(k)$, backscattering amplitude f_i, Debye−Waller factor σ_i, and mean free photoelectron path λ for shell i[43] using a XDAP 2.2.7 code:[29]

$$A_i(k) = \frac{N_i}{kR_i^2}|f_i(k)|\exp\left[-2\left(\sigma_i^2 k^2 + \frac{R_i}{\lambda}\right)\right],\ i = \text{Ag} \qquad (12)$$

The N value was 9.0 ± 0.7 before light irradiation and did not change significantly during both light irradiation (8.3−10.0) and after the light was off (10.1 ± 0.7; Figure 5A). N values of 9−10 correspond to a particle size (d) of 2.5−3.7 nm assuming the spherical face-centered cubic (fcc) nanoparticle model and that surface dispersion (D) is 0.54−0.36 (mean value = 0.45).[44,45]

The σ value was calculated to be 0.00995 nm for Ag metal at 290 K using the correlated Debye model[46,47] with the ab initio multiple-scattering calculation code, FEFF8[48] and the Debye Ag temperature [$\theta_{D(Bulk)}$ 225 K].[49] The XDAP code provides an experimental difference for the σ^2 value from that of the Ag metal (model) based on eq 12. Initial σ values of 0.0101 nm for Ag (3.0 wt %)−ZrO_2 before light irradiation quickly increased to 0.0107 nm (10 min irradiation) and progressively increased to 0.0117 nm (90 min light irradiation, shown in Figure 5B). Then, the value quickly decreased to 0.0101 nm after the light was turned off at 112 min.

Furthermore, we evaluated the temperature at the Ag site based on the σ values. The σ value temperature dependence

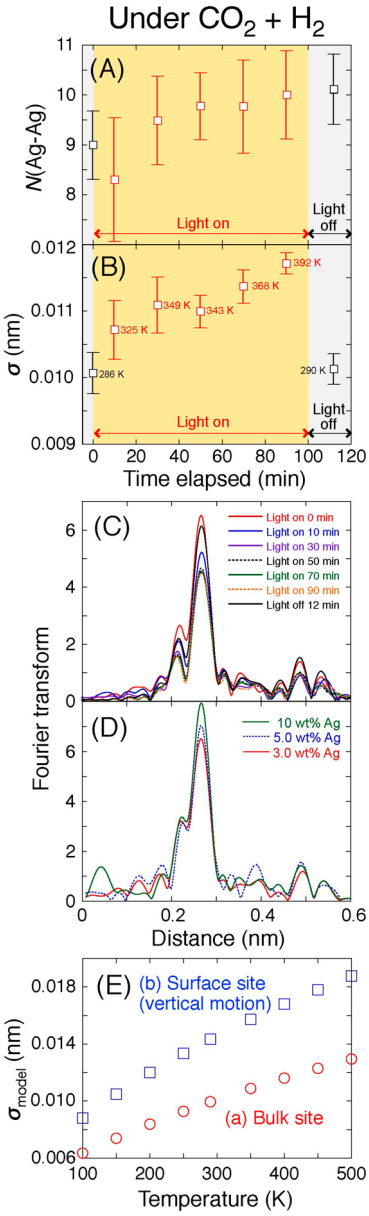

Figure 5. Time course changes of (A) coordination number N values, (B) Debye−Waller factor σ values, and (C) FT obtained from angular photoelectron wavenumber k^3-weighted Ag K-edge EXAFS χ-function for Ag (3.0 wt %)−ZrO_2 under CO_2 (2.3 kPa) and H_2 (21.7 kPa) irradiated by UV−visible light for 100 min followed by dark conditions for 20 min. (D) The change in the FT of the Ag K-edge EXAFS for fresh Ag−ZrO_2: 3.0, 5.0, and 10 wt % Ag. (E) The correlation between the σ value and temperature for bulk sites (circle, ○) and surface sites (vertical motion; square, □) in/on the Ag metal generated by the correlated Debye model using a FEFF8 code.

derives from the FEFF8 combined with the correlated Debye model[46,47] for both bulk and surface Ag sites using the bulk and surface Debye temperature (Figure 5E-a and b, respectively). We assumed that the thermodynamically stable fcc(1 1 1) face had preferable exposure for latter value [$\theta_{D(Surf,\perp)}$ 155 K].[50] We also approximated the mean Ag nanoparticle temperature as the arithmetic mean temperature based on the $\theta_{D(Surf,\perp)}$ weighted by $1/2{\cdot}1/3D$ [D: dispersion of nanoparticles (0.45), for an effective vertical degree of freedom at a free hemisphere surface] and that based on the $\theta_{D(Bulk)}$ weighted by $(1 - D) + 1/2D + 1/2{\cdot}2/3D$ (bulk site, nonfree

DOI: 10.1021/jacs.8b13894
J. Am. Chem. Soc. 2019, 141, 6292−6301

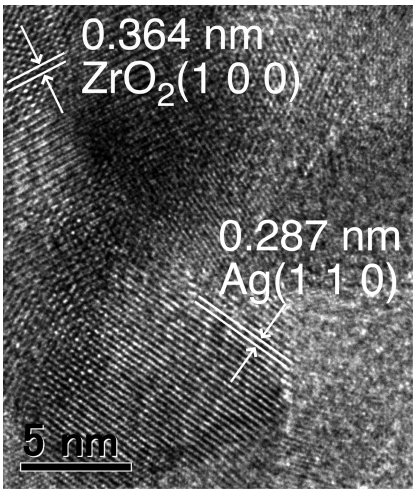

Figure 6. HR-TEM image of Ag (5.0 wt %)−ZrO_2.

hemisphere in contact with ZrO_2, and two lateral degrees of freedom at a free hemisphere surface) (see Supporting Information for the detail).

As a result, the initial temperature of 286 K before irradiation rose to 325 K after 10 min of irradiation and progressively increased to 392 K after 90 min of light irradiation (Figure 5B and Table S2a). The temperature quickly dropped to 290 K after the light was turned off. Such rise/drop in temperature is possibly due to LSPR heat transformation.[51] Similarly to the result using Ag (3.0 wt %)−ZrO_2 above, the initial temperature increased to 363 K after a 90 min UV−visible light irradiation and quickly dropped to 297 K once the light was off using the Ag (5.0 wt %)−ZrO_2 sample (Table S2c). Related to the EXAFS method, the nanoparticle temperature was also monitored based on surface-enhanced Raman scattering for the N≡C stretching vibration of adsorbed probe molecules.[52] The method based on the σ value used in this study via EXAFS is common and can directly probe for all nanoparticles to expose LSPR, e.g., Au and Ag. Three-dimensional mapping of Ag nanoparticles was performed via electron energy loss spectroscopy as a function of energy loss.[53]

Furthermore, we also observed increases or decreases in temperature under argon and UV−visible light (367 K at 50 min of light, 302 K 10 min after light had been turned off; Figure S6B and Table S2b), demonstrating that the ambient gas was not a major factor for temperature up/down. The σ value/temperature negligibly changed until 329 K when the incident light wavelength was filtered at more than 580 nm (Table S2e), whereas an essentially identical rise/drop during full light (365 K at 90 min, 298 K when light was off) for the σ value/temperature was observed when λ was more than 320 nm (Table S2d), demonstrating the heating effect by infrared portion of light were marginal in comparison to that by light whose wavelength was in the range $320 < \lambda < 580$ nm via LSPR of Ag (Figures 4 and S1). Reaction heat was not a factor in this study because the reaction that reduces CO_2 to CO (eq 2) is endothermic. The heating and reaction promotion was reported for the exothermic formation of methane from CO_2 using Ni-based photocatalysts.[31] The temperature dropped to the same level (i.e., 290−302 K) essentially in 10−35 min after UV and/or visible light turned off (Table S2a−e) in comparison to 286 K before UV and/or visible light irradiation. This fact guarantees that the heat originating from probe synchrotron X-ray was negligible in this study.

Ag nanoparticles were always metallic for the Ag−ZrO_2 samples (Figure 5D), and N values for the fresh Ag−ZrO_2 samples gradually increased from 9.0 ± 0.7, 9.6 ± 0.6, and 10.7 ± 0.8 for 3.0, 5.0, and 10 wt % Ag, respectively, which corresponds to (d, D) sets of (2.5 nm, 0.54), (3.1 nm, 0.43), and (4.2 nm, 0.28).[44,45] Thus, Ag surface atoms increase from 0.15 to 0.20 and finally to 0.26 mmol g_{cat}^{-1}, respectively, whereas the CO formation rates reached maximum values at 5.0 wt % Ag (Table 1A and Figure S3), which indicates that the ZrO_2 sites were primarily responsible for CO_2 reduction and were assisted by heated neighboring Ag sites via LSPR that activated and supplied H to move forward eq 2 (Scheme 1d). The close correlation between Au LSPR and H_2 activation was reported using the Au−SiO_2 photocatalyst due to the charge excitation to the antibonding H_2 orbital from LSPR.[54] H_2 activation via the Ni−H species above the Ni/SiO_2·Al_2O_3 photocatalyst[31] relates to the mechanisms discussed in this study, i.e., endothermic CO formation, versus exothermic methane formation.[31]

In the Ag−ZrO_2 UV−visible absorption spectrum, peaks appear centered at 428 and 368 nm (2.90−3.37 eV) due to a LSPR at Ag (Figure 4). The Ag work function is 4.52−4.74 eV,[55] i.e., a Fermi level (E_F) of 0.08−0.30 V for a standard hydrogen electrode versus the reduction potential from CO_2 to CO (−0.11 V)[1] or ZrO_2 conduction band minimum (−1.0 V).[13] For nanoparticles to exhibit LSPR behavior, it was previously reported that the following mechanisms need to occur: (i) charge excitation to an unoccupied adsorbate state,[54,56] (ii) hot electron injection that originates from LSPR for support,[19,57−60] (iii) electron trapping from the support to the Schottky barrier,[59] and (iv) plasmonic resonant energy transfer (PRET).[59−61] However, for cases i−iii, it is often difficult to explain how holes remained react after electron activation/reaction because the O moiety that derives from CO_2 must transfer to the LSPR nanoparticles for oxidation. In this study, H_2 oxidizes based on its association with the reduction of bicarbonate species above ZrO_2. Therefore, holes react with H_2 to form H^+ and must further react with O that derives from CO_2 to form water above the Ag surface. Thus, Ag thermally contributes for CO generation when heated to 325 K−392 K (Figure 5B), i.e., converted from LSPR (H_2 easily dissociates on the heated Ag surface and spills over the ZrO_2 surface) (Scheme 1d,e).

The conversion of LSPR over Ag and Au owing to heat preceded phenol decomposition[62] and thiosulfate oxidation,[63] whereas previous studies considered that short-lived heat converted from LSPR over Ag promotes reactant diffusion in the aqueous solution.[64] This study is the first to report the conversion of CO_2 assisted by heat that was converted via LSPR. Peaks due to formate species were not detected in our FTIR spectra, and we are unable to find evidence that the formate was an intermediate to CO.[14,65] The H and bicarbonate species coupled with the hole and electron, respectively, and combine to form CO and water, which is enhanced by a factor of 3.9 due to Ag (Table 1A-a,d). The rise in the Ag temperature in the ∼0.5 h experiment via LSPR (Figure 5B) and H_2 activation effects (Scheme 1) agree with the ∼0.5 h induction period for CO formation using Ag-containing photocatalysts (Figure S2, Left).

Finally, we tested the photocatalytic conversion of CO_2 using moisture (eq 3). Using ZrO_2, $^{13}CO_2$ (2.3 kPa), moisture

DOI: 10.1021/jacs.8b13894
J. Am. Chem. Soc. 2019, 141, 6292−6301

(2.7 kPa), and UV−visible light, the CO generation rate increased by a factor of 1.2 compared with using $^{13}CO_2$ and H_2 (Table 1A-a, B-a). However, the molar ratio of the newly formed CO:H_2 was 1:0.41 rather than 1:1 based on eq 3. Since 90% of the newly formed CO was ^{12}CO, the bidentate bicarbonate species c was more stable above ZrO_2 (Scheme 1), forming CO gas and a hydroxy group. Conversely, using the Ag (5.0 wt %)−ZrO_2 photocatalyst, the CO formation rate was suppressed by 96% compared with the formation rate when using ZrO_2 (Table 1B-a,b) and by 99% when using CO_2 and H_2 (Table 1A-d). Instead, H_2 preferably formed at 0.15 μmol h^{-1} g_{cat}^{-1}. Based on the effects of Ag, H_2 selectivity in the reduced products increased from 29% to 95% with eq 1 (water splitting) rather than eq 3 due to the preferential adsorption of water versus CO_2 on ZrO_2 and H_2 desorption above Ag (Scheme S1). Water that blocks the O vacancy site is also plausible. Once reaction intermediates, i.e., H and bicarbonate form under light, CO and H_2 are slowly formed via thermal energy under dark at 295 K (Table S1C-a′). In contrast that ^{12}CO was preferably formed among total CO under light (61%; Table 1B-b and Figure S7, Left column), ^{13}CO became a major product (68%, Table S1C-a′ and Figure S7, Right column) under dark due to the gradual consumption of preadsorbed bicarbonate (^{12}C 98.9%) that is in the equilibrium with gas-phase $^{13}CO_2$ (Figure 2B). The addition of Mg^{2+} onto the Ag (5.0 wt %)−ZrO_2 to attract CO_2 to the surface mitigated the water blocking problem. Therefore, the CO formation rate increased from 0.0080 to 0.093 μmol h^{-1} g_{cat}^{-1}, i.e., a factor of 11.7, via the addition of Mg^{2+} similar to the MgO−Pt−TiO_2 photocatalysts (Table 1B-c).[66]

4. CONCLUSIONS

In this study, the Ag (5.0 wt %)−ZrO_2 photocatalyst was the most active during $^{13}CO_2$ reduction using H_2 and UV−visible light at a rate of 0.66 μmol h^{-1} g_{cat}^{-1}. The product included 5.5−8.6% ^{12}CO. However, this CO derives from preadsorbed CO_2 from the air that exchanged with gas-phase $^{13}CO_2$ at a rate constant of 2.0 h^{-1}. FTIR spectra demonstrated bridging and monodentate bicarbonate species via ZrO_2 surface hydroxy group consumption under photoreaction CO_2 and/or H_2 conditions. The bridging bicarbonate species were exchangeable with the gas-phase CO_2 and O vacancy on the ZrO_2 surface should have participated in its formation. Under H_2 and UV−visible light with the expense of bridging bicarbonate, 15% was directed to ^{13}CO formation, whereas the remaining proportion reversely desorbed $^{13}CO_2$.

The charge separation contribution at the ZrO_2 BG and the Ag contribution characterized by LSPR were evaluated based on in-profile kinetic data measurements using sharp-cut filters: 70 and 28%, respectively. We further investigated the contribution of the mean 2.5−3.7 nm Ag nanoparticles using in situ EXAFS. A rise in temperature from 286 to 392 K when exposed to UV−visible light irradiation and a rapid drop to 290 K under dark conditions were directly monitored based on the Debye−Waller factor change for a Ag−Ag interatomic pair interference. H_2 should oxidize based on its association with bicarbonate species reduction above ZrO_2, but no evidence for available O on Ag was found in this study. Thus, the heated Ag surface activated H_2, and the H atoms spill over to the bicarbonate species above ZrO_2 rather than hot electron injection or PRET to/with ZrO_2.

Such dual roles for light during charge separation at the BG and heat via LSPR were remarkably effective when using CO_2 and H_2. Instead, we found that using CO_2 and moisture disadvantageously yielded reversely formed H_2 over Ag. However, H_2 formation was redirected toward CO formation via the addition of Mg^{2+} as the CO_2-anchor sites. The combination of alkaline [earth] metal ion−LSPR metal (Ag, Au)−ZrO_2 is required for artificial photosynthesis free from C-impurity problems and using the dual roles of light: charge separation and heat via LSPR.

■ ASSOCIATED CONTENT

Supporting Information

The Supporting Information is available free of charge on the ACS Publications website at DOI: 10.1021/jacs.8b13894.

Intensity distribution of Xe arc lamp, detailed data from the photocatalytic tests and data from control experiments, absorption−fluorescence spectra, theoretical details and synchrotron X-ray experiments under Ar, a summary of the Ag temperature evaluation based on the Debye−Waller factor, and time course as well as the proposed reaction mechanisms under CO_2 and moisture (PDF)

■ AUTHOR INFORMATION

Corresponding Author

*yizumi@faculty.chiba-u.jp

ORCID

Yasuo Izumi: 0000-0001-8366-1864

Author Contributions

YI, HZ, TI, and TK contributed equally.

Notes

The authors declare no competing financial interest.

■ ACKNOWLEDGMENTS

The authors are grateful for financial support from the Grant-in-Aid for Scientific Research C (17K05961) from the Japan Society for the Promotion of Science, Grant for Academic Research from the Japan Gas Association (2018), and Leading Research Promotion Program (2015−2019) from the Institute for Global Prominent Research, Chiba University. X-ray absorption experiments were performed with the approval of the Photon Factory Proposal Review Committee (2016G577, 2018G649). The authors thank Dr. K. Niki, Department of Chemistry, Chiba University, for helpful discussion on LSPR. The authors would like to thank Enago (www.enago.jp) for the English language review.

■ REFERENCES

(1) Izumi, Y. Recent advances in photocatalytic conversion of carbon dioxide into fuels with water and/or hydrogen using solar energy and beyond. *Coord. Chem. Rev.* **2013**, *257*, 171−186.

(2) Izumi, Y. Recent Advances (2012−2015) in the Photocatalytic Conversion of Carbon Dioxide to Fuels Using Solar Energy: Feasibility for a New Energy. In *Advances in CO_2 Capture, Sequestration, and Conversion*; Jin, F., He, L.-N., Hu, Y. H., Eds.; ACS Books: Washington, D.C., 2015; Chapter 1, Vol. *1194*, pp 1−46.

(3) Li, K.; Peng, B.; Peng, T. Recent Advances in Heterogeneous Photocatalytic CO_2 Conversion to Solar Fuels. *ACS Catal.* **2016**, *6*, 7485−7527.

(4) Grigioni, I.; Dozzi, M. V.; Bernareggi, M.; Chiarello, G. L.; Selli, E. Photocatalytic CO_2 Reduction vs. H_2 Production: The Effects of Surface Carbon-Containing Impurities on the Performance of TiO_2-Based Photocatalysts. *Catal. Today* **2017**, *281*, 214−220.

DOI: 10.1021/jacs.8b13894
J. Am. Chem. Soc. 2019, 141, 6292−6301

(5) Yui, T.; Kan, A.; Saitoh, C.; Koide, K.; Ibusuki, T.; Ishitani, O. Photochemical Reduction of CO_2 Using TiO_2: Effects of Organic Adsorbates on TiO_2 and Deposition of Pd onto TiO_2. *ACS Appl. Mater. Interfaces* **2011**, *3*, 2594−2600.
(6) Yang, C. C.; Yu, Y.-H.; van der Linden, B.; Wu, J. C. S.; Mul, G. Artificial Photosynthesis over Crystalline TiO_2-Based Catalysts: Fact or Fiction? *J. Am. Chem. Soc.* **2010**, *132*, 8398−8406.
(7) Teramura, K.; Tanaka, T. Necessary and Sufficient Conditions for the Successful Three-Phase Photocatalytic Reduction of CO_2 by H_2O over Heterogeneous Photocatalysts. *Phys. Chem. Chem. Phys.* **2018**, *20*, 8423−8431.
(8) Wang, S.; Hou, Y.; Wang, X. Development of a Stable $MnCo_2O_4$ Cocatalyst for Photocatalytic CO_2 Reduction with Visible Light. *ACS Appl. Mater. Interfaces* **2015**, *7*, 4327−4335.
(9) Kar, P.; Zeng, S.; Zhang, Y.; Vahidzadeh, E.; Manuel, A.; Kisslinger, R.; Alam, K. M.; Thakur, U. K.; Mahdi, N.; Kumar, P.; Shankar, K. High Rate CO_2 Photoreduction Using Flame Annealed TiO_2 Nanotubes. *Appl. Catal., B* **2019**, *243*, 522−536.
(10) Ulagappan, N.; Frei, H. Machanistic Study of CO_2 Photoreduction in Ti Silicalite Molecular Sieve by FT-IR Spectroscopy. *J. Phys. Chem. A* **2000**, *104*, 7834−7839.
(11) Hameed, Y.; Gabidullin, B.; Richeson, D. Photocatalytic CO_2 Reduction with Manganese Complexes Bearing a κ^2-PN Ligand: Breaking the α-Diimine Hold on Group 7 Catalysts and Switching Selectivity. *Inorg. Chem.* **2018**, *57*, 13092−13096.
(12) Boston, D. J.; Xu, C.; Armstrong, D. W.; MacDonnell, F. M. Photochemical Reduction of Carbon Dioxide to Methanol and Formate in a Homogeneous System with Pyridinium Catalysts. *J. Am. Chem. Soc.* **2013**, *135*, 16252−16255.
(13) Lo, C.-C.; Hung, C.-H.; Yuan, C.-S.; Wu, J.-F. Photoredution of Carbon Dioxide with H_2 and H_2O over TiO_2 and ZrO_2 in a Circulated Photocatalytic Reactor. *Sol. Energy Mater. Sol. Cells* **2007**, *91*, 1765−1774.
(14) Yoshida, S.; Kohno, Y. A New Type of Photocatalysis Initiated by Photoexcitation of Adsorbed Carbon Dioxide on ZrO_2. *Catal. Surv. Jpn.* **2001**, *4*, 107−114.
(15) Kohno, Y.; Tanaka, T.; Funabiki, T.; Yoshida, S. Photoreduction of Carbon Dioxide with Hydrogen over ZrO_2. *Chem. Commun.* **1997**, *33*, 841−842.
(16) Ahmed, N.; Shibata, Y.; Taniguchi, T.; Izumi, Y. Photocatalytic Conversion of Carbon Dioxide into Methanol Using Zinc−Copper−M(III) (M = Aluminum, Gallium) Layered Double Hydroxides. *J. Catal.* **2011**, *279*, 123−135.
(17) Kawamura, S.; Zhang, H.; Tamba, M.; Kojima, T.; Miyano, M.; Yoshida, Y.; Yoshiba, M.; Izumi, Y. Efficient Volcano-type Dependence of Photocatalytic CO_2 Conversion into Methane Using Hydrogen at Reaction Pressures up to 0.80 MPa. *J. Catal.* **2017**, *345*, 39−52.
(18) Zhang, H.; Kawamura, S.; Tamba, M.; Kojima, T.; Yoshiba, M.; Izumi, Y. Is Water More Reactive Than H_2 in Photocatalytic CO_2 Conversion into Fuels Using Semiconductor Catalysts under High Reaction Pressures? *J. Catal.* **2017**, *352*, 452−465.
(19) Tian, Y.; Tatsuma, T. Mechanism and Applications of Plasmon-Induced Charge Separation at TiO_2 Films Loaded with Gold Nanoparticles. *J. Am. Chem. Soc.* **2005**, *127*, 7632−7637.
(20) Kawamura, S.; Ahmed, N.; Carja, G.; Izumi, Y. Photocatalytic Conversion of Carbon Dioxide Using Zn−Cu−Ga Layered Double Hydroxides Assembled with Cu Phthalocyanine: Cu in Contact with Gaseous Reactant is Needed for Methanol Generation. *Oil Gas Sci. Technol.* **2015**, *70*, 841−852.
(21) Urushidate, K.; Matsuzawa, S.; Nakatani, L.; Li, J.; Kojima, T.; Izumi, Y. Solar Cell with Photocatalyst Layers on Both the Anode and Cathode Providing an Electromotive Force of Two Volts per Cell. *ACS Sustainable Chem. Eng.* **2018**, *6*, 11892−11903.
(22) Zhang, H.; Izumi, Y. Why Is Water More Reactive Than Hydrogen in Photocatalytic CO_2 Conversion at Higher Pressure? Elucidation by Means of X-Ray Absorption Fine Structure and Gas Chromatography-Mass Spectrometry. *Front. Chem.* **2018**, *6*, 408.
(23) Wein, L. A.; Zhang, H.; Urushidate, K.; Miyano, M.; Izumi, Y. Optimized Photoreduction of CO_2 Exclusively into Methanol Utilizing Liberated Reaction Space in Layered Double Hydroxides Comprising Zinc, Copper, and Gallium. *Appl. Surf. Sci.* **2018**, *447*, 687−696.
(24) Morikawa, M.; Ahmed, N.; Yoshida, Y.; Izumi, Y. Photoconversion of Carbon Dioxide in Zinc−Copper−Gallium Layered Double Hydroxides: The Kinetics to Hydrogen Carbonate and Further to CO/Methanol. *Appl. Catal., B* **2014**, *144*, 561−569.
(25) Ogura, Y.; Okamoto, S.; Itoi, T.; Fujishima, Y.; Yoshida, Y.; Izumi, Y. A Photofuel Cell Comprising Titanium Oxide and Silver(I/0) Photocatalysts for Use of Acidic Water as a Fuel. *Chem. Commun.* **2014**, *50*, 3067−3070.
(26) Bearden, J. A. X-Ray Wavelengths. *Rev. Mod. Phys.* **1967**, *39*, 78−124.
(27) Yoshida, Y.; Itoi, T.; Izumi, Y. Preferential Photooxidation of CO in Hydrogen across the Crystalline Face Boundary over Spheroidal ZnO Promoted by Cu Ions. *J. Phys. Chem. C* **2015**, *119*, 21585−21598.
(28) Yoshida, Y.; Mitani, Y.; Itoi, T.; Izumi, Y. Preferential Oxidation of Carbon Monoxide in Hydrogen Using Zinc Oxide Photocatalysts Promoted and Tuned by Adsorbed Copper Ions. *J. Catal.* **2012**, *287*, 190−202.
(29) Vaarkamp, M.; Linders, H.; Koningsberger, D. *XDAP Version 2.2.7.*; XAFS Services International: Woudenberg, The Netherlands, 2006.
(30) Liu, L. G.; Bassett, W. A. Compression of Ag and Phase Transformation of NaCl. *J. Appl. Phys.* **1973**, *44*, 1475−1479.
(31) Sastre, F.; Puga, A. V.; Liu, L.; Corma, A.; García, H. Complete Photocatalytic Reduction of CO_2 to Methane by H_2 under Solar Light Irradiation. *J. Am. Chem. Soc.* **2014**, *136*, 6798−6801.
(32) Puigdollers, A. R.; Illas, F.; Pacchioni, G. Structure and Properties of Zirconia Nanoparticles from Density Functional Theory Calculations. *J. Phys. Chem. C* **2016**, *120*, 4392−4402.
(33) Dou, M.; Zhang, M.; Chen, Y.; Yu, Y. Theoretical Study of Methanol Synthesis from CO_2 and CO Hydrogenation on the Surface of ZrO_2 Supported In_2O_3 Catalyst. *Surf. Sci.* **2018**, *672-673*, 7−12.
(34) Lin, J.; Ma, C.; Wang, Q.; Xu, Y.; Ma, G.; Wang, J.; Wang, H.; Dong, C.; Zhang, C.; Ding, M. Enhanced Low-Temperature Performance of CO_2 Methanation over Mesoporous Ni/Al_2O_3-ZrO_2 Catalysts. *Appl. Catal., B* **2019**, *243*, 262−272.
(35) Li, W.; Nie, X.; Jiang, X.; Zhang, A.; Ding, F.; Liu, M.; Liu, Z.; Guo, X.; Song, C. ZrO_2 Support Imparts Superior Activity and Stability of Co Catalysts for CO_2 Methanation. *Appl. Catal., B* **2018**, *220*, 397−408.
(36) Takano, H.; Kirihata, Y.; Izumiya, K.; Kumagai, N.; Habazaki, H.; Hashimoto, K. Highly active Ni/Y-doped ZrO_2 catalysts for CO_2 methanation. *Appl. Surf. Sci.* **2016**, *388*, 653−663.
(37) Solis-Garcia, A.; Louvier, J. F.; Almendarez, A.; Fierro, J. C. Participation of Surface Bicarbonate, Formate and Methoxy Species in the Carbon Dioxide Methanation Catalyzed by ZrO_2-Supported Ni. *Appl. Catal., B* **2017**, *218*, 611−620.
(38) Warren, D. S.; McQuillan, A. J. Influence of Adsorbed Water on Phonon and UV-Induced IR Absorption of TiO_2 Photocatalytic Particle Films. *J. Phys. Chem. B* **2004**, *108*, 19373−19379.
(39) Wu, K.; Chen, J.; McBride, J. R.; Lian, T. Efficient Hot-Electron Transfer by a Plasmon-Induced Interfacial Charge-Transfer Transition. *Science* **2015**, *349*, 632−635.
(40) Dunwell, M.; Lu, Q.; Heyes, J. M.; Rosen, J.; Chen, J. G.; Yan, Y.; Jiao, F.; Xu, B. The Central Role of Bicarbonate in the Electrochemical Reduction of Carbon Dioxide on Gold. *J. Am. Chem. Soc.* **2017**, *139*, 3774−3783.
(41) Joo, J.; Yu, T.; Kim, Y. W.; Park, H. M.; Wu, F.; Zhang, J. Z.; Hyeon, T. Multigram Scale Synthesis and Characterization of Monodisperse Tetragonal Zirconia Nanocrystals. *J. Am. Chem. Soc.* **2003**, *125*, 6553−6557.
(42) Teufer, G. The Crystal Structure of tetragonal ZrO_2. *Acta Crystallogr.* **1962**, *15*, 1187.

DOI: 10.1021/jacs.8b13894
J. Am. Chem. Soc. 2019, 141, 6292−6301

(43) Lee, P. A.; Citrin, P. H.; Eisenberger, P.; Kincaid, B. M. Extended X-Ray Absorption Fine Structure − Its Strengths and Limitations as a Structural Tool. *Rev. Mod. Phys.* **1981**, *53*, 769−806.
(44) Kip, B. J.; Duivenvoorden, F. B. M.; Koningsberger, D. C.; Prins, R. Determination of Metal Particle Size of Highly Dispersed Rh, Ir, and Pt Catalysts by Hydrogen Chemisorption and EXAFS. *J. Catal.* **1987**, *105*, 26−38.
(45) Humbolt, F.; Didillon, D.; Lepeltier, F.; Candy, J. P.; Corker, J.; Clause, O.; Bayard, F.; Basset, J. M. Surface Organometallic Chemistry on Metals: Formation of a Stable ≡Sn(n-C_4H_9) fragment as a Precursor of Surface Alloy Obtained by Stepwise Hydrogenolysis of Sn(n-C_4H_9)$_4$ on a Platinum Particle Supported on Silica. *J. Am. Chem. Soc.* **1998**, *120*, 137−146.
(46) Beni, G.; Platzman, P. M. Temperature and Polarization Dependence of Extended X-Ray Absorption Fine-Structure Spectra. *Phys. Rev. B* **1976**, *14*, 1514−1518.
(47) Sevillano, E.; Meuth, H.; Rehr, J. J. Extended X-Ray Absorption Fine Structure Debye−Waller Factors. I. Monoatomic Crystals. *Phys. Rev. B: Condens. Matter Mater. Phys.* **1979**, *20*, 4908−4911.
(48) Ankudinov, L.; Ravel, B.; Rehr, J. J.; Condradson, S. D. Real-Space Multiple-Scattering Calculation and Interpretation of X-Ray-Absorption Near-Edge Structure. *Phys. Rev. B: Condens. Matter Mater. Phys.* **1998**, *58*, 7565−7576.
(49) Gray, D. E., Ed.; *American Institute of Physics Handbook*, 3rd ed.; McGraw-Hill: New York, 1972; pp 4−116.
(50) Morabito, J. B., Jr.; Steiger, R. F.; Somorjai, G. A. Studies of the Mean Displacement of Surface Atoms in the (1 0 1) and (1 1 0) Faces of Silver Single Crystals at Low Temperatures. *Phys. Rev.* **1969**, *179*, 638−644.
(51) Ma, J.; Wang, Z.; Wang, L.-W. Interplay between Plasmon and Single-Particle Excitations in a Metal Nanocluster. *Nat. Commun.* **2015**, *6*, 10107.
(52) Yang, H.; He, L.-Q.; Hu, Y.-W.; Lu, X.; Li, G.-R.; Liu, B.; Ren, B.; Tong, Y.; Fang, P.-P. Quantitative Detection of Photothermal and Photoelectrocatalytic Effects Induced by SPR from Au@Pt Nanoparticles. *Angew. Chem., Int. Ed.* **2015**, *54*, 11462−11466.
(53) Nicoletti, O.; de la Peña, F.; Leary, R. K.; Holland, D. J.; Ducati, C.; Midgley, P. A. Three-Dimensional Imaging of Localized Surface Plasmon Resonances of Metal Nanoparticles. *Nature* **2013**, *502*, 80−84.
(54) Mukherjee, S.; Zhou, L.; Goodman, A. M.; Large, N.; Ayala-Orozco, C.; Zhang, Y.; Nordlander, P.; Halas, N. J. Hot-Electron-Induced Dissociation of H_2 on Gold Nanoparticles Supported on SiO_2. *J. Am. Chem. Soc.* **2014**, *138*, 64−67.
(55) Haynes, W. M., Ed.; *CRC Handbook of Chemistry and Physics*, 96th ed.; CRC Press: Boca Raton, 2015; pp 12−122.
(56) Boerigter, C.; Campana, R.; Morabito, M.; Linic, S. Evidence and Implications of Direct Charge Excitation as the Dominant Mechanism in Plasmon-Mediated Photocatalysis. *Nat. Commun.* **2016**, *7*, 10545.
(57) Clavero, C. Plasmon-Induced Hot-Electron Generation at Nanoparticle/Metal-Oxide Interfaces for Photovoltaic and Photocatalytic Devices. *Nat. Photonics* **2014**, *8*, 95−103.
(58) Chaudhary, D.; Singh, S.; Vankar, V. D.; Khare, N. A Ternary Ag/TiO_2/CNT Photoanode for Efficient Photoelectrochemical Water Splitting Under Visible Light Irradiation. *Int. J. Hydrogen Energy* **2017**, *42*, 7826−7835.
(59) Wei, X.; Shao, C.; Li, X.; Lu, N.; Wang, K.; Zhang, Z.; Liu, Y. Facile In Situ Synthesis of Plasmonic Nanoparticles-Decorated g-C_3N_4/TiO_2 Heterojunction Nanofibers and Comparison Study of Their Photosynergistic Effects for Efficient Photocatalytic H_2 Evolution. *Nanoscale* **2016**, *8*, 11034−11043.
(60) Naldoni, A.; Riboni, F.; Marelli, M.; Bossola, F.; Ulisse, G.; Carlo, A. D.; Piš, I.; Nappini, S.; Malvestuto, M.; Dozzi, M. V.; Psaro, R.; Selli, E.; Dal Santo, V. Influence of TiO_2 Electronic Structure and Strong Metal−Support Interaction on Plasmonic Au Photocatalytic Oxidations. *Catal. Sci. Technol.* **2016**, *6*, 3220−3229.
(61) Cushing, S. K.; Li, J.; Meng, F.; Senty, T. R.; Suri, S.; Zhi, M.; Li, M.; Bristow, A. D.; Wu, N. Photocatalytic Activity Enhanced by Plasmonic Resonant Energy Transfer from Metal to Semiconductor. *J. Am. Chem. Soc.* **2012**, *134*, 15033−15041.
(62) Zhang, Z.; Wang, W.; Gao, E.; Sun, S.; Zhang, L. Photocatalysis Coupled with Thermal Effect Induced by SPR on Ag-Loaded Bi_2WO_6 with Enhanced Photocatalytic Activity. *J. Phys. Chem. C* **2012**, *116*, 25898−25903.
(63) Yen, C.-W.; El-Sayed, M. A. Plasmonic Field Effect on the Hexacyanoferrate(III)−Thiosulfate Electron Transfer Catalytic Reaction on Gold Nanoparticles: Electromagnetic or Thermal? *J. Phys. Chem. C* **2009**, *113*, 19585−19590.
(64) Gao, S.; Zhang, Z.; Liu, K.; Dong, B. Direct Evidence of Plasmonic Enhancement on Catalytic Reduction of 4-Nitrophenol over Silver Nanoparticles Supported on Flexible Fibrous Networks. *Appl. Catal., B* **2016**, *188*, 245−252.
(65) Teramura, K.; Tanaka, T.; Ishikawa, H.; Kohno, Y.; Funabiki, T. Photocatalytic Reduction of CO_2 to CO in the Presence of H_2 or CH_4 as a Reductant over MgO. *J. Phys. Chem. B* **2004**, *108*, 346−354.
(66) Xie, S.; Wang, Y.; Zhang, Q.; Deng, W.; Wang, Y. MgO- and Pt-Promoted TiO_2 as an Efficient Photocatalyst for the Preferential Reduction of Carbon Dioxide in the Presence of Water. *ACS Catal.* **2014**, *4*, 3644−3653.

DOI: 10.1021/jacs.8b13894
J. Am. Chem. Soc. 2019, 141, 6292−6301